nanomaterials

MDPI

Article

Optical Interference and Spectral Thermal Emission in Nanometric Multilayer Coatings: Effects on Admissible Thermal Loads of Nickel-Based Superalloys

Liviu Badea *,† and Mirela Dragan *,†

National Research and Development Institute for Nonferrous and Rare Metals—IMNR (INCDMNR-IMNR), 178-184 Biruinței Blvd., 077145 Pantelimon, Ilfov County, Romania

* Correspondence: lbadea@imnr.ro (L.B.); mirelad.dragan@gmail.com (M.D.)

† These authors contributed equally to this work.

Abstract

Coatings on superalloy components are usually treated as barriers to conduction, yet films a few hundred nanometers thick add negligible conductive resistance and act mainly through the radiative boundary condition. The novelty of this work is to carry coherent, layer-resolved thin-film emission through the surface energy balance to the admissible thermal load under a surface-temperature cap; thin-film emission studies usually stop at the emissivity. A 2 mm Nimonic 80A disk coated with NiCrAlY, Al_2O_3 and rare-earth-doped zirconia (900 nm in total) is analyzed, with the cap at 1050 K. Coherent transfer-matrix optics and layer-resolved Kirchhoff emission are coupled with one- and two-dimensional finite-volume conduction; parametric and structural uncertainties are propagated separately. Interference above the absorbing bond coat raises the total hemispherical emissivity from 0.14 to 0.21. A linearized surface energy balance shows that the gray-body approximation overpredicts the admissible load when the assumed gray emissivity exceeds the spectrally weighted value and the irradiation temperature stays below the cap. Under convection and enclosure irradiation, the load limits vary by a few percent across model variants; under collimated irradiation, they depend strongly on the rim condition, interfacial roughness and bond-coat interband absorption. The results are theoretical and specific to this disk, stack and cap.

Keywords: thermal barrier coatings; thin-film thermal emission; transfer-matrix method; gray-body approximation; admissible thermal load

Check for updates

Academic Editor: Christian Mitterer

Received: 10 November 2026
Revised: 25 November 2026
Accepted: 25 November 2026
Published: 28 November 2026

Copyright: © 2026 by the authors. Licensee MDPI, Basel, Switzerland. This article is an open access article distributed under the terms and conditions of the Creative Commons Attribution (CC BY) license.

1. Introduction

Thermal barrier coatings make it possible for parts manufactured from nickel-based superalloys to operate in gas flows hotter than the melting point of the base alloy. In the conventional system, there is a porous yttria-stabilized zirconia (YSZ) top coat, a thermally grown oxide (TGO) consisting of an alumina scale formed in situ during heat treatment and operation, and a metallic MCrAlY bond coat on the substrate. Such a structure reduces the substrate temperature by several hundred kelvins across a layer only a few hundred micrometers thick [1–3]. Radiative heat transfer plays two roles in this system. Firstly, zirconia is partially transparent in the near-infrared, allowing some of the radiation to penetrate into deeper layers [4,5]. Secondly, the surface optical properties set the radiative exchange with the surroundings. Recent compositions, such as rare-earth high-entropy zirconates [6,7], have been studied mainly for their reduced lattice thermal conductivity,

whereas little is known about their optical constants in the IR. When the oxide layers are only a few hundred nanometers thick, their contribution to the overall resistance becomes comparable to the boundary resistance of their interfaces and is much smaller than that of the bulk substrate [8–11]. Therefore, they no longer insulate the part. However, acting as interference films atop the metallic reflector [12], the stack acquires a different functionality: control of the radiative properties. Whether optical interference changes the thermal load that the part can carry depends on how the interference and phonon modes overlap with the blackbody spectrum of the hot surface. The goal of the present work is therefore to examine theoretically a thin-film stack on a nickel-based alloy and to determine under what conditions these effects modify its admissible thermal load in different environments. The key questions are whether the gray-body approximation is reasonable, how accurate it is, and which parameters introduce uncertainties into the calculations. We consider a 2 mm thick, 15 mm diameter disk of Nimonic 80A coated with a NiCrAlY film 200 nm thick, followed by 500 nm of Al_2O_3 and 200 nm of lanthanum-, samarium-, gadolinium-, neodymium-, and ytterbium-doped zirconia (hereafter HEO-Z). The heating is increased until the surface reaches the critical value T* = 1050 K. The proposed approach combines temperature-dependent dielectric functions with fluctuational electrodynamics [13], accounting for the coherent optical response of the multilayer and for finite-size volumetric heat-conduction effects. The emission is calculated according to the generalized Kirchhoff rule for layered structures with arbitrary nonuniform temperature profiles [14,15]; this formulation is directly connected to the solution method based on Parratt recursions or the transfer-matrix formalism [16–18]. Within this approach, steady states are computed for an enclosure environment, pure forced convection and collimated irradiation, together with transients after a step-wise increase.

Each element of this approach is established; the contribution lies in their coupling. Radiative analyses of barrier coatings usually address thick, semitransparent zirconia layers [4,5,19,20]. Analyses of thin-film and nanophotonic emission [14,15,21], in turn, stop at the emissivity and do not reach the load that a component can sustain. Here the coherent, layer-resolved emission enters the conduction problem under a surface-temperature cap. The admissible load then follows directly from the optical constants, the sign of the gray-body error follows from the radiative regime at the cap, and the parametric and structural uncertainties remain separate for each load case. The results are theoretical and refer to the system defined in Section 2.1.

2. Theoretical Model and Numerical Methods

The model combines three elements: (i) the dielectric functions of the four materials; (ii) the coherent-optics description of the layered structure, which determines the emission and absorption spectra at the free surface; and (iii) the heat-conduction problem in the disk, closed by the surface energy balance at the limit T*. Assumptions are stated where they are introduced, the parameters are collected in Table 1, and the symbols are listed in Table 2.

2.1. Geometry, Load Cases and Admissible Load

The disk has diameter $D = 15$ mm and substrate thickness $L = 2$ mm. Counting from the free surface ($z = 0$, z pointing into the disk), it carries HEO-Z ($d_1 = 200$ nm), Al_2O_3 ($d_2 = 500$ nm) and NiCrAlY ($d_3 = 200$ nm) on Nimonic 80A. The interfaces are planar, specular and optically coherent, and bulk material properties are applied to the films. The admissible load P_{adm} is the largest value of the control parameter P (T_{env}, T_g or q_{irr}) for which the maximum coating temperature does not exceed T^* at steady state; below, it is also called the load limit. In case S1 the disk faces a black enclosure at T_{env}. In S2 a gas at T_g heats the surface through a heat-transfer coefficient h_g representative of a combustor liner

(S2-L) or of a blade (S2-B) [4]. The gas is gray and optically thin, with emissivity $\varepsilon_g = 0$ in the baseline, and the surroundings radiate at $T_w = 300$ K. In S3 a collimated blackbody source at 2000 K irradiates the disk at normal incidence with irradiance q_{irr}. The back face is cooled by a liner condition (BC-L) or a blade condition (BC-B), each combining convection to a coolant at T_c with gray radiation of emissivity ε_{back} to a sink at T_c. The convective values follow Ref. [4]; the interior radiation of BC-B is an assumption of the present study. The suffix -L or -B of a case denotes the back-face condition (e.g., S1-B is the enclosure case with blade cooling); for S2 it also fixes the gas-side coefficient.

2.2. Dielectric Functions

The Al_2O_3 film is described by the four-parameter semi-quantum (FPSQ) factorized form [22], with the temperature-dependent mode parameters measured for corundum between 300 and 928 K [23],

$$\varepsilon_{\perp,\parallel}(\tilde{\nu}, T) = \varepsilon_\infty \prod_j \frac{\Omega_{LO,j}^2 - \tilde{\nu}^2 - i\gamma_{LO,j}\tilde{\nu}}{\Omega_{TO,j}^2 - \tilde{\nu}^2 - i\gamma_{TO,j}\tilde{\nu}}, \quad (1)$$

where $\tilde{\nu}$ is the wavenumber, ε_∞ the high-frequency permittivity, and $\Omega_{TO,j}$, $\Omega_{LO,j}$, $\gamma_{TO,j}$ and $\gamma_{LO,j}$ the transverse and longitudinal mode frequencies and damping constants. With the time dependence $e^{-i\omega t}$, passive media have Im $\varepsilon \geq 0$. The ordinary and extraordinary responses are averaged as $\varepsilon = (2\varepsilon_\perp + \varepsilon_\parallel)/3$, which corresponds to a randomly textured film, and the mode parameters are extrapolated linearly above 928 K. Because the FPSQ product decays too slowly in the multiphonon window, its imaginary part is blended smoothly into that of the equivalent Lorentz-oscillator model above about 1070 cm^{-1}, and the Kramers–Kronig partner of this modification is added to the real part [24]. The blended permittivity is thus causal by construction; the pure FPSQ form is retained as a structural alternative.

No infrared optical constants are available for the HEO-Z composition, so a single-oscillator surrogate of cubic zirconia is used,

$$\varepsilon_1(\tilde{\nu}, T) = \varepsilon_\infty + \frac{\Delta\varepsilon\,\Omega^2(T)}{\Omega^2(T) - \tilde{\nu}^2 - i\gamma(T)\tilde{\nu}}, \quad (2)$$

with $\Omega(T) = \Omega_{300}[1 - b_\Omega(T - 300\text{ K})]$ and $\gamma(T) = g_{300}\Omega_{300}[1 + b_\gamma(T - 300\text{ K})]$. The mode position Ω_{300} is the first-principles cubic T_{1u} frequency [25]. The oscillator strength $\Delta\varepsilon$ places the bulk reflectance minimum at 710–720 cm^{-1}. This interval is a target adopted for the surrogate. Measured infrared optical constants of cubic yttria-doped zirconia, obtained from single-crystal reflectance spectra, are given in [26]. In addition, ε_∞ reproduces the near-infrared refractive index of yttria-stabilized zirconia [27]. The damping ratio g_{300} is an assumption that represents cation and vacancy disorder, and the coefficients b_Ω and b_γ are the median temperature trends of the corundum modes [23]. This surrogate is the weakest optical input.

Both metals are described by a Drude permittivity,

$$\varepsilon_m(\tilde{\nu}) = \varepsilon_{bg} - \frac{\tilde{\nu}_p^2}{\tilde{\nu}^2 + i\gamma\tilde{\nu}}, \quad \gamma = \frac{2\pi c\varepsilon_0\left(100\tilde{\nu}_p\right)^2\rho_e}{100}, \quad (3)$$

with the plasma wavenumber $\tilde{\nu}_p$ of nickel [28]. The second relation is the DC limit of the Drude model, $\sigma_{DC} = \varepsilon_0{\omega_p}^2/\Gamma$, written for wavenumbers in cm^{-1}, the electronic resistivity ρ_e in Ω m and c in m s^{-1}. For the bond coat, $\rho_e = L_0T/(k_{bc} - k_{ph})$ follows from the Wiedemann–Franz law with the Sommerfeld Lorenz number L_0, the thermal conductivity of dense vacuum-plasma-sprayed NiCrAlY [29] and a lattice contribution k_{ph} estimated from Nimonic 80A. The combined uncertainty of the conductivity and lattice estimates

defines a Wiedemann–Franz interval for γ_{bc}, of which three representative values, 2715, 3018 and 3434 cm^{-1}, are shown in the figures. The substrate damping follows from the Nimonic 80A resistivity [30]. Interband absorption of nickel [31] is omitted in the baseline and treated as a structural variant (Drude + IB).

Table 1. Main model parameters. The intervals used in the uncertainty analysis are given in Table S1.

Parameter	Symbol	Value	Unit	Source
Disk diameter; substrate thickness	D; L	15; 2	mm	Model input
Film thicknesses (HEO-Z, Al_2O_3, NiCrAlY)	d_1, d_2, d_3	200, 500, 200	nm	Model input
Surface cap; initial temperature	T^*; T_0	1050; 300	K	Model input
Al_2O_3 phonon parameters (300–928 K)	$\Omega_{TO,j}$, $\Omega_{LO,j}$	tabulated	cm^{-1}	[23]; extrapolated above 928 K
HEO-Z high-frequency permittivity; strength	ε_∞; $\Delta\varepsilon$	4.47; 23.0	–	Fitted to [27]; cf. [26]
HEO-Z mode position; damping ratio	Ω_{300}; g_{300}	258; 0.10	cm^{-1}; –	[25]; assumption
HEO-Z thermal coefficients	b_Ω; b_γ	3.4×10^{-5}; 3.6×10^{-3}	K^{-1}	Derived from [23]
Metal plasma wavenumber; background	$\tilde{\nu}_p$; ε_{bg}	39 400; 1	cm^{-1}; –	[28]; assumption
Lorenz number (Sommerfeld)	L_0	2.443×10^{-8}	W Ω K^{-2}	Free-electron value
Bond-coat damping at 1050 K (interval)	γ_{bc}	3018 (2469–3434)	cm^{-1}	Wiedemann–Franz with [29]
Substrate damping at 1050 K	γ_{sub}	3399	cm^{-1}	From resistivity [30]
Thermal conductivity HEO-Z; Al_2O_3	k_1; k_2	1.2; 7	W m^{-1} K^{-1}	Assumption (bulk range [6,32])
Thermal conductivity NiCrAlY (296–1223 K)	k_3	11 → 30	W m^{-1} K^{-1}	[29]
Thermal conductivity Nimonic 80A (293–1273 K)	k_4	11.2 → 28.4	W m^{-1} K^{-1}	[30]
Density HEO-Z; Al_2O_3; NiCrAlY; Nimonic	ρ	7130; 3978; 7711; 8190	kg m^{-3}	[6,29,30,32]
Specific heat HEO-Z; Al_2O_3	c_p	457; 857	J kg^{-1} K^{-1}	Dulong–Petit; [32]
Specific heat NiCrAlY; Nimonic	c_p	455 → 789; 448 → 703	J kg^{-1} K^{-1}	[30,33]
Boundary resistances	R_1; R_2; R_3	5×10^{-9}; 5×10^{-9}; 1×10^{-9}	m^2 K W^{-1}	Assumption; ranges [10,11,34]
Gas-side coefficient (S2-L; S2-B)	h_g	250; 3014	W m^{-2} K^{-1}	[4]
Coolant coefficient; temperature (BC-L; BC-B)	h_c; T_c	110, 800; 3768, 1000	W m^{-2} K^{-1}; K	[4]
Back-face emissivity (sink at T_c)	ε_{back}	0.6	–	[4] (BC-L); assumption (BC-B)
Rim emissivity (two-dimensional scenario)	ε_{rim}	0.6	–	Scenario
Gas emissivity; wall temperature	ε_g; T_w	0 (0.6 variant); 300	–; K	Scenario; assumption

2.3. Coherent Optics and Layer-Resolved Emission

For each wavenumber, direction cosine $\mu = \cos\theta$ and polarization $p \in \{s, p\}$, the amplitude reflection of the stack follows from the Parratt recursion [16,17],

$$\Gamma_j = \frac{r_{j,j+1} + \Gamma_{j+1}\exp\left(2ik_{z,j+1}d_{j+1}\right)}{1 + r_{j,j+1}\Gamma_{j+1}\exp\left(2ik_{z,j+1}d_{j+1}\right)},\ R_p = |\Gamma_0|^2, \tag{4}$$

which starts from the semi-infinite substrate ($\Gamma_4 = 0$) and proceeds toward the ambient medium 0. Here $r_{j,j+1}$ is the Fresnel coefficient of interface j, $k_{z,j} = (\varepsilon_j {k_0}^2 - \beta^2)^{1/2}$ the normal wave vector on the branch $\mathrm{Im}\, k_{z,j} \geq 0$, $k_0 = 2\pi\cdot 100\tilde{\nu}$ and $\beta = k_0 \sin\theta$. The fields inside the layers are reconstructed from bottom-up local reflection ratios, in which every factor is bounded, so the reconstruction remains stable for any value of $\mathrm{Im}(k_z d)$. The absorptance A_m of a sublayer m is the difference in the normalized Poynting flux at its boundaries [18]. Because the substrate is opaque, energy conservation and the generalized Kirchhoff law [14] give the directional spectral emissivity

$$\varepsilon_{\tilde{\nu},\mu,p} = 1 - R_p = \sum_m A_{m,p} + A_{\mathrm{sub},p}. \tag{5}$$

Equation (5) is applied sublayer by sublayer under the assumption of local thermodynamic equilibrium, so that a sublayer at temperature T_m emits in proportion to its absorptance. The emitted intensity is

$$I_{\tilde{\nu}}(\mu) = \frac{1}{2}\sum_{p=s,p}\left[\sum_m A_{m,p}(\tilde{\nu},\mu) I_\mathrm{b}(\tilde{\nu}, T_m) + A_{\mathrm{sub},p} I_\mathrm{b}(\tilde{\nu}, T_\mathrm{sub})\right], \tag{6}$$

where I_b is the Planck intensity per unit wavenumber. Equation (6) is the indirect form of fluctuational electrodynamics; its equivalence with the direct, source-based form [13,15] was checked numerically (Section 2.6). The total hemispherical emissivity and the source-weighted absorptance follow from hemispherical and Planck averages,

$$\varepsilon_\mathrm{h}(T) = \frac{1}{\sigma T^4}\int_0^\infty \pi\left[2\int_0^1 \bar{\varepsilon}_{\tilde{\nu},\mu}\mu\,\mathrm{d}\mu\right] I_\mathrm{b}(\tilde{\nu}, T)\,\mathrm{d}\tilde{\nu},\ \Phi = \frac{\alpha(\mathrm{src})}{\varepsilon_\mathrm{h}(T_\mathrm{s})}, \tag{7}$$

where $\bar{\varepsilon}$ is the polarization average and $\alpha(\mathrm{src})$ the absorptance of the stack for the spectrum and geometry of the source: normal-incidence absorptance for the collimated load S3, hemispherical absorptance for diffuse irradiation. The spectral mismatch Φ equals 1 for a gray surface. It measures how far absorption and emission differ at the level of total quantities, which is a property of the spectra and not a departure from Kirchhoff's law. The integral is normalized by σT^4, and the parts of the Planck spectrum outside the grid are added analytically [35] (Equation (S1)).

2.4. Heat Conduction

Conduction in the disk is described in conservative enthalpy form [36] in axisymmetric coordinates,

$$\frac{\partial H(T)}{\partial t} = \frac{1}{r}\frac{\partial}{\partial r}\left(rk(T)\frac{\partial T}{\partial r}\right) + \frac{\partial}{\partial z}\left(k(T)\frac{\partial T}{\partial z}\right) + S_\mathrm{rad},\ H(T) = \rho\int_{300\,\mathrm{K}}^{T} c_\mathrm{p}(T')\,\mathrm{d}T', \tag{8}$$

where the density ρ is constant and S_rad is the volumetric radiative source of the resolved coating (zero in the reduced model). Writing H as the integral of c_p, rather than as $\rho c_\mathrm{p}(T)T$, keeps $\mathrm{d}H/\mathrm{d}T = \rho c_\mathrm{p}$ exact for any $c_\mathrm{p}(T)$. The flux $q_z = -k\partial T/\partial z$ is continuous across each interface, while T jumps by $T(z_j^-) - T(z_j^+) = R_j q_z$ at the thermal boundary resistances R_1–R_3 [8]. The reduced model lumps the coating into $R_\mathrm{coat} = \Sigma d_j/k_j + \Sigma R_j$, evaluated at T^*, and applies at the two faces

$$q_z(0) = h_\mathrm{g}\left(T_\mathrm{g} - T_\mathrm{s}\right) + q^a - \varepsilon_\mathrm{h}(T_\mathrm{s})\sigma T_\mathrm{s}^4,\ q_z(L) = h_\mathrm{c}(T_\mathrm{b} - T_\mathrm{c}) + \varepsilon_\mathrm{back}\sigma\left(T_\mathrm{b}^4 - T_\mathrm{c}^4\right), \tag{9}$$

where q^{a} is the absorbed radiative flux, T_s and T_b the surface and back-face temperatures; $q_z(0)$ is the net flux entering the disk and $q_z(L)$ the flux leaving it. The axis is a symmetry line, and the rim is either adiabatic (one-dimensional model) or gray, $-k\partial T/\partial r = \varepsilon_{rim}\sigma(T^4 - {T_{amb}}^4)$ with $T_{amb} = 300$ K (two-dimensional model). The rim treatment is a scenario, not a calibrated condition. The disk starts from $T_0 = 300$ K.

2.5. Admissible Load, Gray-Model Error and Characteristic Scales

At steady state, P_{adm} is obtained without time marching. With the surface at T^*, q_b and T_b follow from the back-face condition of Equation (9) and from the Kirchhoff transform of steady one-dimensional conduction in the substrate [37],

$$K(T^* - R_{coat}q_b) - K(T_b) = q_b L,\ K(T) = \int_{T_{ref}}^{T} k(T')\,dT', \tag{10}$$

which is exact for any $k(T)$. The flux q_b depends on the back-face condition but not on the surface optics. The top balance $F(P) = q_b$ is then solved for the load parameter P. For S2, $F = h_g(T_g - T^*) + \alpha G - \varepsilon_h\sigma T^{*4}$, where G is the hemispherical irradiation; for S3 the absorbed collimated flux $\alpha(\mathrm{src})q_{irr}$ replaces the convective term. A gray description replaces every α and ε by a single ε_{gray}. Subtracting the two balances and expanding to first order in $P_{gray} - P_{FE}$ gives

$$P_{gray} - P_{FE} \approx -\frac{(\alpha_{gray} - \alpha)G - (\varepsilon_{gray} - \varepsilon_h)\sigma T^{*4}}{\overline{F}_P} = -\frac{(\varepsilon_{gray} - \varepsilon_h)\sigma T^{*4}\Theta_G}{\overline{F}_P}\ (\Phi = 1), \tag{11}$$

where FE denotes the nongray (fluctuational-electrodynamics) model, $\overline{F}_P$ the mean of $\partial F/\partial P$ for both, and $\Theta_G = (T_G/T^*)^4 - 1$, with $T_G = (G/\sigma)^{1/4}$ the irradiation temperature at the limit. For S2, $\overline{F}_P = h_g + \bar{\alpha}\partial G/\partial T_g$ is positive, so an emissivity larger than ε_h overpredicts P_{adm} if and only if $T_G < T^*$, that is, when the surface is a net radiative emitter at the cap. For S2-L with $\varepsilon_g = 0$, $G = \sigma {T_w}^4$ does not depend on T_g, $\overline{F}_P = h_g$, and Equation (11) is exact; it gives the same error as the nonlinear solver (Section 3.6). The relation is an elementary linearization of the top balance, and we use it as an interpretive tool.

Two further scales are used below. The relative error of evaluating the emission at T_s instead of the resolved profile of the coating is bounded by $\Xi = 4qR_{coat}/T_s$, with q the flux crossing the coating. Linearizing the boundary fluxes about the limit state gives the lumped thermal time of the disk,

$$\tau_{th} = \frac{\left(\rho c_p\right)_{sub}L + \sum_j \left(\rho c_p\right)_j d_j}{h_g + 4\varepsilon_h\sigma T_s^3 + h_c + 4\varepsilon_{back}\sigma T_b^3}, \tag{12}$$

where the coating term in the numerator is retained for completeness although it is about 3×10^{-4} of the substrate term.

The symbols used in the equations and figures are defined in Table 2, together with their SI units; where the text quotes a quantity in practical units, such as wavenumbers in cm^{-1}, the conversion is stated where it first appears.

Table 2. Notation. Spectroscopic quantities are quoted in cm^{-1} in the text; the SI unit is given here.

Symbol	Physical Meaning	SI Unit
z, r	depth below the free surface, radius	m
d_j, L, D	film thickness, substrate thickness, disk diameter	m
λ, $\tilde{\nu}$	vacuum wavelength, wavenumber (quoted in cm^{-1})	m, m^{-1}

Table 2. *Cont.*

Symbol	Physical Meaning	SI Unit
θ, μ	polar angle in vacuum, $\mu = \cos\theta$	rad, –
ε_j	complex relative permittivity of layer j	–
γ_{bc}, γ_{sub}	Drude damping of bond coat and substrate	m^{-1}
δ_{pow}	power skin depth $\lambda/(4\pi\kappa)$, κ extinction index	m
R_p, A_m, A_{sub}	reflectance (polarization p), sublayer and substrate absorptance	–
$\varepsilon_{\mathrm{n},\nu}$, $\varepsilon_{\mathrm{h},\nu}$, ε_{h}	normal and hemispherical spectral emissivity, total hemispherical emissivity	–
$\alpha(\mathrm{src})$, Φ	source absorptance, spectral mismatch $\alpha(\mathrm{src})/\varepsilon_{\mathrm{h}}$	–
I_{b}, $E_{\mathrm{b},\lambda}$	Planck intensity, blackbody spectral emissive power	$\mathrm{W\,m^{-2}\,sr^{-1}\,m}$, $\mathrm{W\,m^{-3}}$
T, T_{s}, T_{b}, T^*	temperature: general, surface, back face, cap	K
T_{g}, T_{env}, T_{src}	gas, enclosure and source temperature	K
T_{G}, Θ_{G}	irradiation temperature, $(T_{\mathrm{G}}/T^*)^4 - 1$	K, –
q_{b}, q_{irr}, q^{a}, G	back-face flux, collimated irradiance, absorbed flux, irradiation	$\mathrm{W\,m^{-2}}$
P, P_{adm}	load parameter (T_{env}, T_{g} or q_{irr}), admissible value	K or $\mathrm{W\,m^{-2}}$
h_{g}, h_{c}	gas-side and coolant-side heat-transfer coefficient	$\mathrm{W\,m^{-2}\,K^{-1}}$
ε_{g}, $\varepsilon_{\mathrm{back}}$, $\varepsilon_{\mathrm{rim}}$, $\varepsilon_{\mathrm{gray}}$	gas, back-face, rim and gray-model emissivity	–
k, ρ, c_{p}, H	conductivity, density, specific heat, volumetric enthalpy	$\mathrm{W\,m^{-1}\,K^{-1}}$, $\mathrm{kg\,m^{-3}}$, $\mathrm{J\,kg^{-1}\,K^{-1}}$, $\mathrm{J\,m^{-3}}$
R_j, R_{coat}	thermal boundary resistance, coating resistance	$\mathrm{m^2\,K\,W^{-1}}$
τ_{th}, t_{cross}	lumped thermal time, time at which max T reaches T^*	s
Ξ, S_{T}	bound on the non-isothermal emission correction, total Sobol index	–

2.6. Numerical Implementation and Verification

The spectral grid spans 20–50 000 $\mathrm{cm^{-1}}$ and is refined to 1 $\mathrm{cm^{-1}}$ across the oxide phonon bands; angular integrals use 16 Gauss–Legendre nodes in μ. The optics are tabulated between 300 and 1200 K and interpolated linearly. Conduction is discretized with cell-centered finite volumes [38], with 10, 25 and 10 sublayers in the three films of the resolved coating and 30 radial columns in the two-dimensional disk. Transients are integrated with the variable-step second-order backward differentiation formula (BDF2), started with one implicit Euler step [39], with Newton-linearized radiation; Richardson estimates on refined grids place the time-discretization error of the histories at about 0.5 K or less. Steady states

are Picard-iterated on $\varepsilon_h(T_s)$. Physical constants are the CODATA 2018 values [40], and all calculations were run in GNU Octave 8.4.

The implementation was verified against independent references: Fresnel and Airy solutions; the optical closure $R + \Sigma A_m + A_{sub} = 1$, satisfied to about 10^{-12}; the equivalence of the direct and indirect emission densities, to the same level; a steady composite wall with boundary resistances; and the Carslaw–Jaeger series for a convectively cooled slab [37] (Figure S2). The observed orders of accuracy are 2 in space and 1 and 2 for implicit Euler and Crank–Nicolson time stepping; the production BDF2 scheme shows order 2.0 for uniform and geometrically graded steps against the same series solution. Doubling the number of radial columns changes the two-dimensional limits by less than 10^{-5}. A uniform radial grid underestimates T in the outermost coating cells by a few kelvin, a first-order artifact of the half-cell at the rim; these cells are excluded from the maxima, and a graded grid shows that the effect on P_{adm} is about 10^{-6}. The three-dimensional fields in Figure S1 are rotations of the axisymmetric solution, exact for axisymmetric loads, and not an independent three-dimensional simulation.

2.7. Uncertainty Quantification

Parametric uncertainty is propagated by Monte Carlo sampling ($N = 2000$) of 15 independent, uniformly distributed factors (Table S1). Two priors are compared for γ_{bc}: the Wiedemann–Franz interval and a wide interval that also covers departures of the Lorenz number from L_0. Total Sobol indices of eight factors are estimated with the Saltelli design and the Jansen estimator [41–43] (Equation (S4)) at a base sample of 128. At this sample size, the error of the indices on analytic benchmarks is 0.05–0.14, so only well-separated factors are ranked. The Monte Carlo bands are conditional on the assumed intervals. Structural alternatives (rim treatment, roughness, interband terms, Al_2O_3 wing), which have no probability distribution, are reported separately as variants (Table S2).

3. Results

The results proceed from length scales and spectra to load limits and transients. Unless stated otherwise, the optics are evaluated at 1050 K with the central Wiedemann–Franz damping $\gamma_{bc} = 3018\ cm^{-1}$, and the one-dimensional reduced model with an adiabatic rim is used.

3.1. Length and Time Scales

Whether a 0.9 µm stack can affect a 2 mm disk depends on how its length and time scales compare with those of the substrate and of the radiation field. The substrate is more than three orders of magnitude thicker than the stack (Figure 1a), and across the Al_2O_3 property range the stack adds only 0.2–0.6% to the substrate resistance (panel c). It cannot act as a conductive barrier. The optical scales are reversed. We measure the opacity of the bond coat by the power skin depth $\delta_{pow} = 1/(2k_0\kappa)$, over which the absorbed power, not the field amplitude, decays by 1/e. It approaches the relaxation limit of Equation (3), about 20 nm, at short wavelengths and grows as $\lambda^{1/2}$ in the Hagen–Rubens regime (panel b). Even for the largest damping it stays below d_3 between 0.3 and 30 µm, where almost all of the 1050 K Planck power lies, so the bond coat is an opaque reflector. Panel (d) contains two distinct time scales. The local diffusion time $\Delta z^2/\alpha$ of each film is below a microsecond and justifies isothermal films and quasi-static optics. The lumped time τ_{th} of Equation (12), between about 1.5 and 33 s, describes the response of the whole disk and sets the duration of the transients. The stack is thus nearly transparent to conduction but can change the radiative boundary condition strongly.

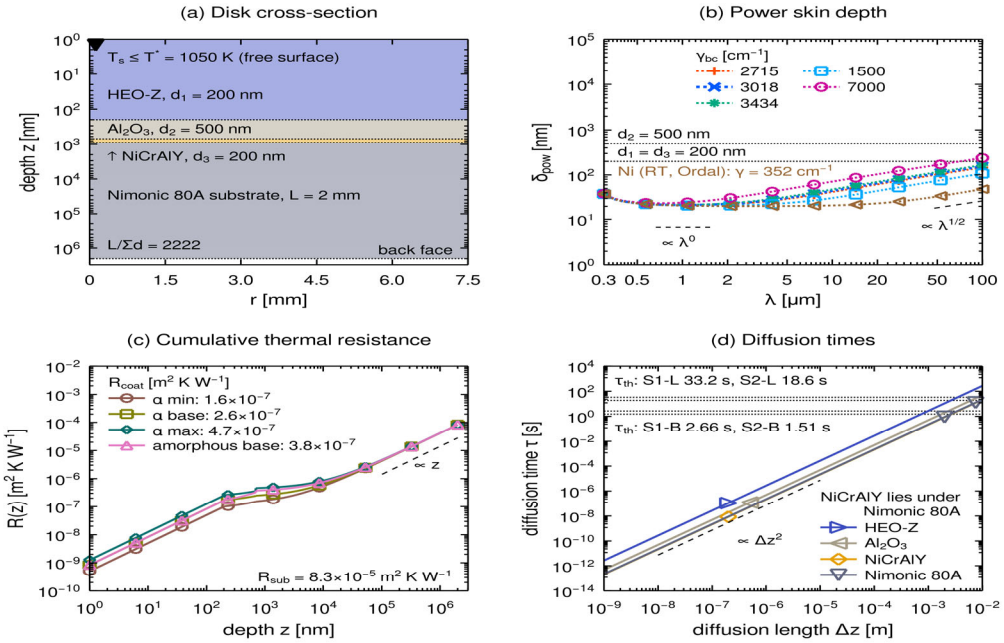

Figure 1. Length and time scales of the coated disk at 1050 K: (**a**) cross-section (logarithmic depth); (**b** bond-coat power skin depth δpow for γbc = 1500–7000 cm^{-1} (dotted: film thicknesses); (**c**) cumulative thermal resistance R(z); (**d**) diffusion times $\Delta z^2/\alpha$ and lumped times τ_{th}.

Within the stack, about two thirds of the resistance lies in the HEO-Z film, which has the lowest conductivity, and less than a twentieth in the three boundary resistances. The whole stack is thus equivalent to roughly 7 μm of substrate at the cap, so its conductive weight is set by the oxide conductivities rather than by the interfaces; doubling all three boundary resistances would raise it by only about 4%.

3.2. Origin of the Emissivity Enhancement

If the stack is thermally transparent, its influence must be carried by the emissivity, and adding the films one at a time isolates the mechanism. The curves are normal spectral emissivities, whereas the legends give the total hemispherical ε_h, which includes the Planck weighting and the angular integral. The dotted Planck curve only marks where the emission weight lies. The bare Drude metal has a featureless emissivity that decreases with wavelength (Figure 2a). Either oxide alone raises ε_h from 0.14 to 0.22 (panels b and c): a dielectric spacer on a lossy reflector creates interference maxima in which the field at the metal, and with it the absorption there, is enhanced. The full stack gains a factor of 1.44 but stays slightly below either single film (panel d), because its first-order maximum λ_1, the longest-wavelength interference maximum, lies farther from the Planck peak. The quarter-wave estimate $4\Sigma n_j d_j$, with indices at 5 μm, falls 10% short of λ_1. It assumes an ideal reflector and nondispersive films; the computed position contains both the reflection phase of the metal and the oxide dispersion, which are not separated here. The bond coat supplies about 90% of the emitted power, so the oxides act through interference rather than through their own emission. Interband terms raise ε_h by about a fifth (from 0.206 to 0.252), more than the spread due to γ_{bc}.

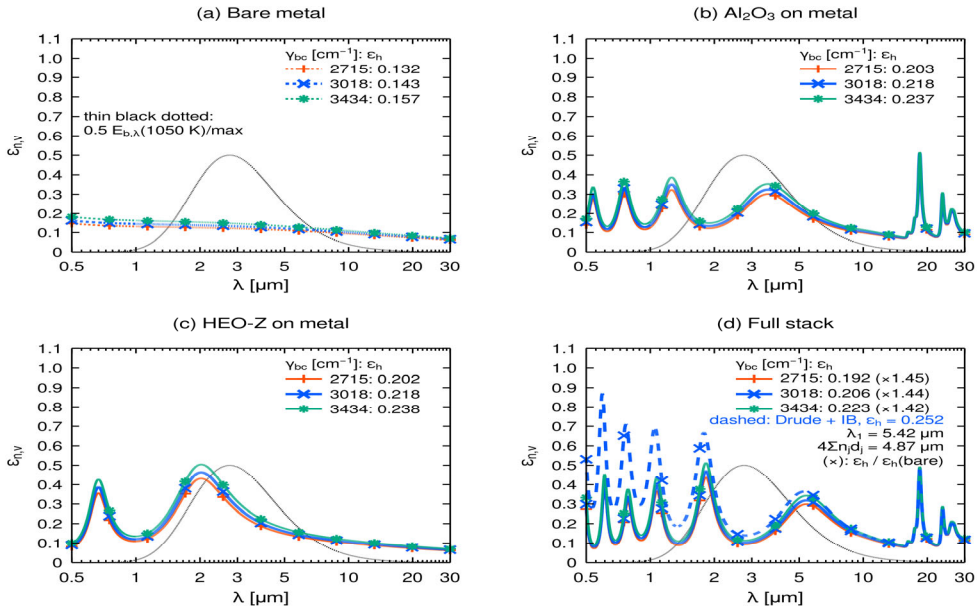

Figure 2. Build-up of the normal spectral emissivity $\varepsilon_{n,\nu}$ at 1050 K for γ_{bc} = 2715, 3018 and 3434 cm^{-1}; legends: total hemispherical ε_h. (**a**) Bare NiCrAlY/Nimonic 80A. (**b**) 500 nm Al_2O_3 on the metal. (**c**) 200 nm HEO-Z on the metal. (**d**) Full stack, with $\varepsilon_h/\varepsilon_h$(bare) in parentheses and Drude + interband (IB) dashed; λ_1: first-order maximum. Dotted: $0.5E_{b,\lambda}(1050\ K)/max$, for orientation only. The colored dotted lines with markers in (**a**) are the bare-metal spectra.

The enhancement is an admittance-matching effect. An opaque metal reflects most of the infrared power because its optical admittance greatly exceeds that of air; a transparent spacer of optical thickness close to an odd multiple of $\lambda/4$ transforms this admittance and lowers the reflectance. Because the bond coat is opaque, each reduction in the reflectance reappears by Equation (5) as absorption in the stack, mostly in the metal skin, and hence as emission. The gain is therefore bounded by the overlap of the Planck spectrum with the interference maxima.

Interference affects the admissible load through the same mechanism. At an interference maximum, the waves reflected at the oxide interfaces and at the metal cancel partially, as in thin absorbing coatings on metals [44]. The stack reflects less, and the metal skin absorbs, and hence emits, more (Equation (5)). Only the radiative terms of the top balance in Equation (9) change. The flux that the substrate carries at the cap is set by the back face and is independent of the optics (Equation (10)). The phonon modes act mainly through the dispersion of the oxides. Their reststrahlen bands fall in the long-wavelength tail of the Planck spectrum at the cap (Section 3.4). Where most of the power is emitted, the oxides are nearly transparent, and their refractive indices fix the positions of the interference orders. Phonon absorption terminates the interference at long wavelengths (Section 3.3), and the *p*-polarized Al_2O_3 feature (Section 3.5) adds little to ε_h.

The baseline stack is not an emissivity optimum. Either oxide alone gives a slightly higher ε_h (Figure 2b,c), and the thickness map peaks at $d_2 = 0$ (Figure S1d). The sequence reproduces, at nanometric thickness, the architecture of a conventional coating system: a top oxide, an alumina scale and an MCrAlY bond coat (Section 1). The alumina layer is required by this system. The relevant comparison is therefore between the coated and the bare metal.

3.3. Role of the Bond Coat and of the Interference Order

Figure 3 tests the two roles of the bond coat assumed in Figure 2, opaque layer and reflector. Panel (a) shows the net radiative flux reaching the substrate per unit wavelength,

divided by the conducted flux q_b, so the ratio has units of μm^{-1}; its integral, given in the legend, is a few 10^{-4} at the limit states. It is positive when external radiation leaks through the bond coat (S1-L, S3-L) and negative when the substrate only emits toward cold surroundings (S2), and it is irrelevant for the heat balance. Panel (b) shows that the substrate absorptance decays as $\exp(-d_3/\delta)$ with the power skin depth of Figure 1b. The reflectance saturates accordingly: for $d_3 \geq 100$ nm ε_h changes by less than 10^{-3}, whereas thinner bond coats alter it. The first-order wavelength grows linearly with d_2 (panel c), with slopes below the nondispersive value $4n_2$ that decrease as HEO-Z is added, and saturates near 10 µm, where Al_2O_3 begins to absorb. With increasing angle λ_1 moves to shorter wavelengths (panel d). The phase-thickness estimate, with θ_j from Snell's law, neglects the angular change in the reflection phase and is drawn only where it agrees within 10%. For the thickest alumina film, the order merges with the *p*-polarized Al_2O_3 band near 11 µm. Above about 100 nm of bond coat, the oxide thicknesses are therefore the optical design variables (Figure S1).

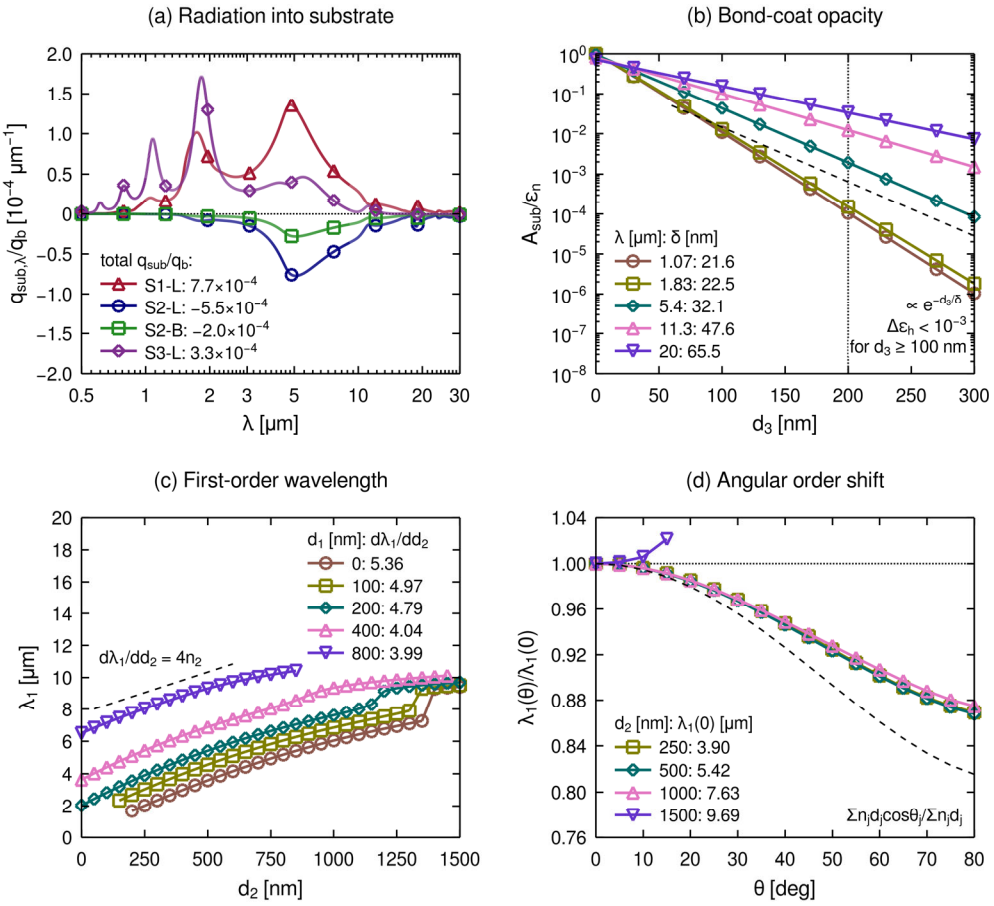

Figure 3. Bond coat and interference order at 1050 K ($\gamma_{bc} = 3018$ cm^{-1}). (**a**) Net radiative flux into the substrate per unit wavelength, $q_{sub,\lambda}/q_b$ [μm^{-1}], at four limit states; legend: integrated q_{sub}/q_b. (**b**) A_{sub}/ε_n at normal incidence versus d_3 for five wavelengths (legend: δ); dashed: $\exp(-d_3/\delta)$. (**c**) λ_1 versus d_2 for $d_1 = 0$–800 nm (legend: fitted slope); dashed: $4n_2$. (**d**) $\lambda_1(\theta)/\lambda_1(0)$ for $d_2 = 250$–1500 nm; dashed: $\Sigma n_j d_j \cos\theta_j / \Sigma n_j d_j$ for $d_2 = 500$ nm. Dotted lines: zero net flux in (**a**), the nominal $d_3 = 200$ nm in (**b**) and $\lambda_1(\theta)/\lambda_1(0) = 1$ in (**d**).

3.4. Temperature Dependence of the Emission

Two temperatures enter the emission through different mechanisms: the optics temperature T_{opt} changes the phonon damping and the electronic resistivity, and the emission temperature T_e alters the Planck weighting. The spectral emissivity keeps its structure

over 300–1200 K (Figure 4a). Panel (b) shows the density per unit wavenumber, $\varepsilon_{h,\nu} I_b(\tilde{\nu})$, plotted against λ. A density per unit wavelength carries the Jacobian $|d\tilde{\nu}/d\lambda| = 10^4/\lambda^2$ and peaks at shorter wavelengths: at 1050 K near 1.8 µm, instead of 4.8 µm. In this convention, the maximum moves from the Al_2O_3 phonon feature to the first interference order above about 850 K. Band fractions do not depend on the convention. At the cap, about half of the power lies between 2 and 5 µm and less than a tenth above 10 µm (panel c); the five fractions add up to unity within 0.3%. Panel (d) gives the Planck-weighted hemispherical emissivity of optics at T_{opt}; only the diagonal $T_e = T_{opt}$ enters the heat balance. At $T_e = 1050$ K, the full range of T_{opt} changes ε_h by less than 0.01, whereas at fixed optics T_e moves it through a maximum near 600 K. The Planck weighting thus controls this dependence. The Al_2O_3 parameters are extrapolated above 928 K; four alternative extrapolations shift ε_h at the cap by at most 0.001.

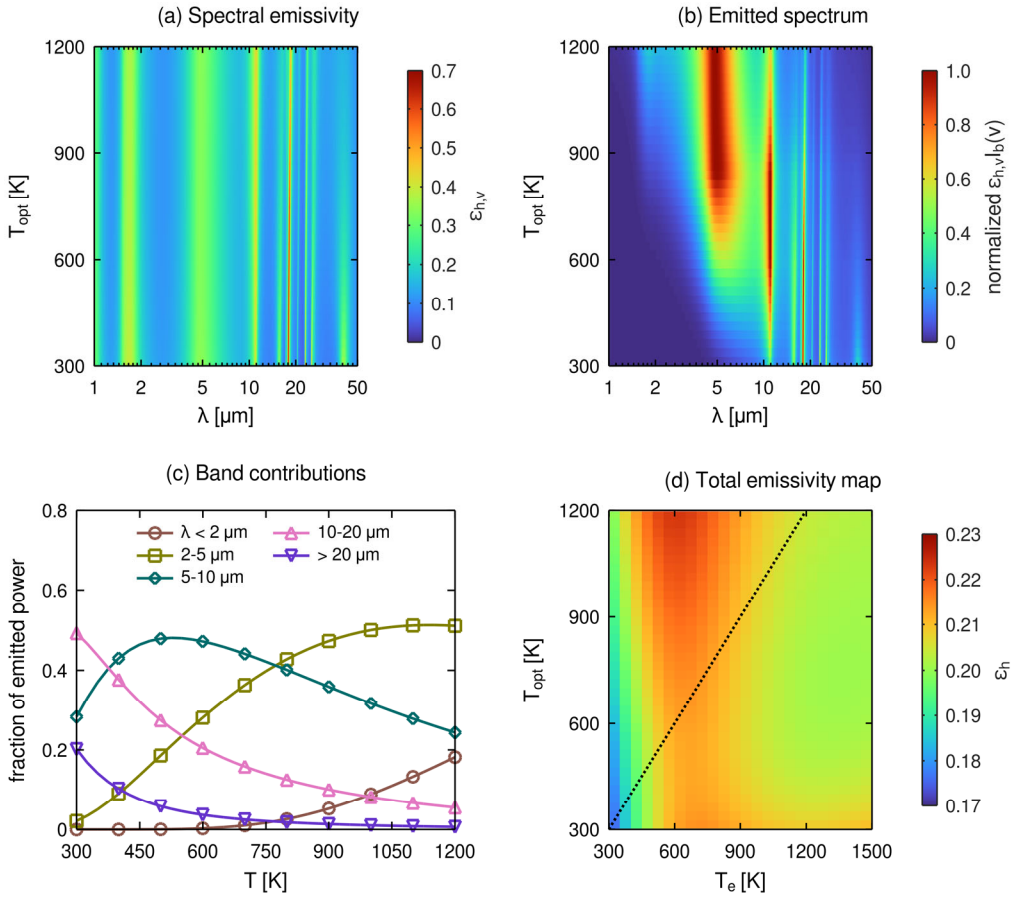

Figure 4. Temperature dependence of the emission ($\gamma_{bc} = 3018$ cm^{-1}, hemispherical quantities). (**a**) Spectral emissivity $\varepsilon_{h,\nu}(\lambda, T_{opt})$. (**b**) Emitted density per unit wavenumber, $\varepsilon_{h,\nu} I_b(\tilde{\nu}, T)$, normalized to its maximum in each row and plotted against λ. (**c**) Fraction of the emitted power in five wavelength bands ($T_e = T_{opt}$). (**d**) $\varepsilon_h(T_e$; optics at $T_{opt})$; dotted: $T_e = T_{opt}$.

3.5. Directional and Polarized Emission

The load limits rest on hemispherical quantities, so their accuracy depends on how the emission is distributed in angle and polarization. At 1050 K, the interference orders move to shorter wavelengths with increasing θ, and a sharp ridge near 10–11 µm strengthens at oblique angles (Figure 5a). It is a p-only feature, with ε_p close to unity and ε_s small (panel b), located near the frequency at which the real part of the alumina permittivity crosses zero. This is the signature of the Berreman mode of thin polar films [45]; we use the attribution qualitatively. Panel (c) gives, for each direction, the band shares of the power emitted in that

direction, normalized over 1–50 µm, which holds 99.8% of σT^4. Toward grazing angles, the weight shifts from 5 to 10 µm to 2–5 µm, following the orders. In panel (d), $I(\theta)$ is the power emitted per unit solid angle and per unit area of the emitting surface, so that $\pi I(\theta)/\sigma T^4 = \varepsilon(\theta) \cos\theta$; the intensity of the whole face follows by multiplication with its area. The distribution is close to Lambertian at 1050 and 1200 K but lies below it near the normal, because $\varepsilon(\theta)$ rises away from the normal. Using the normal emissivity instead of ε_h would underestimate the emitted flux by about 4% at the cap and 20% at 300 K. Hemispherical integration is necessary, while the angular redistribution is a minor correction.

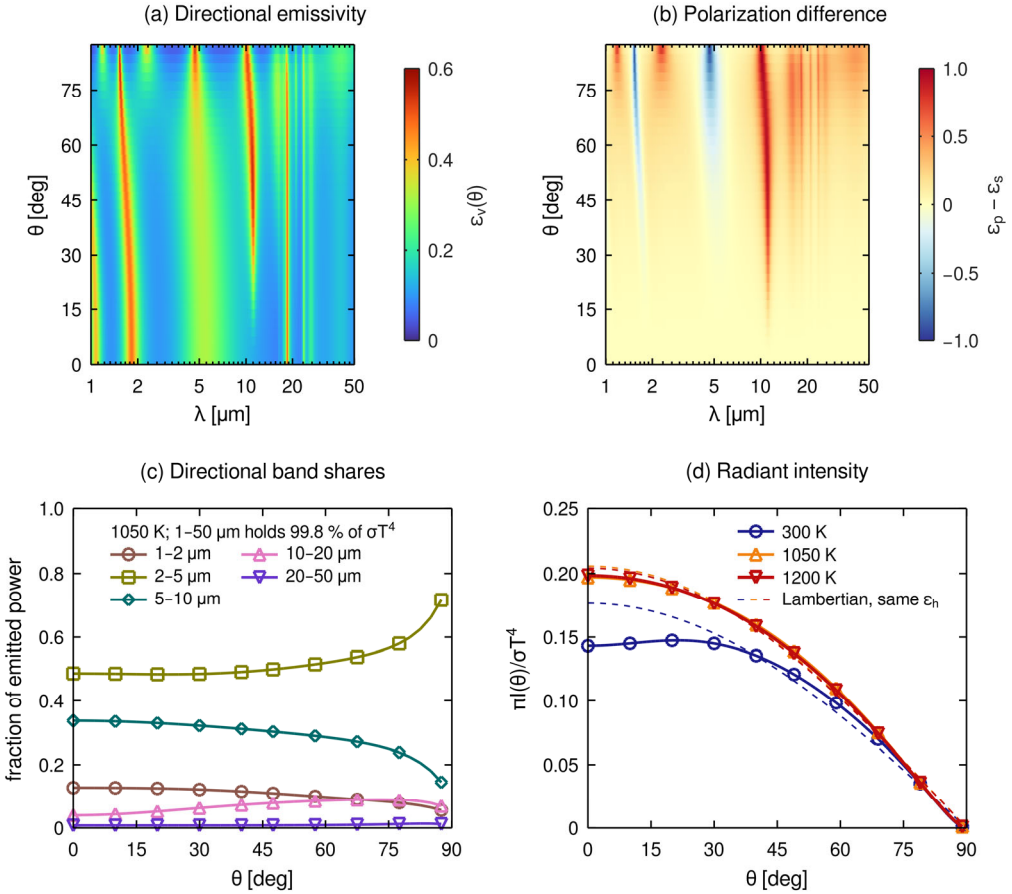

Figure 5. Directional emission of the full stack ($\gamma_{bc} = 3018\ \mathrm{cm}^{-1}$). (**a**) Unpolarized directional spectral emissivity at 1050 K. (**b**) $\varepsilon_p - \varepsilon_s$ at 1050 K. (**c**) Band shares of the power emitted in direction θ at 1050 K, normalized over 1–50 µm. (**d**) Emission per unit solid angle and unit surface area, $\pi I(\theta)/\sigma T^4 = \varepsilon(\theta) \cos\theta$, at 300, 1050 and 1200 K; dashed: Lambertian emitter with the same ε_h. In (**d**), each Lambertian curve has the color of the corresponding temperature.

Angular effects matter mainly when the surroundings do not fill the hemisphere. A surface that exchanges radiation through a narrow port, or faces a cooled wall over a limited cone, is governed by the directional emissivity averaged over that cone rather than by ε_h. Because the normal and hemispherical values differ by about 4% at the cap, such an average would change the limits very little; the *p*-polarized ridge near 11 µm matters only for strongly oblique viewing.

3.6. Error of Gray-Body Admissible Loads

We define the gray-body error as $\Delta P = P_{gray} - P_{FE}$, the limit computed with a single value for both emission and absorption minus the spectral one. Positive ΔP admits a load that drives the real coating above the cap and is non-conservative. Because P is T_{env} for S1-L,

T_g for the convective cases and q_{irr} for S3-L, Figure 6a compares relative deviations and panel (b) gives the shift in T_g in kelvin. The sign follows the radiative regime, measured by Θ_G in Equation (11). All curves cross zero at $\varepsilon_{gray} = \varepsilon_h$. For the liner with a transparent gas the surface is a net emitter ($\Theta_G \approx -1$), and $\varepsilon_{gray} = 0.9$ overpredicts the limiting gas temperature by 190 K (14%). With an emitting gas the same choice is slightly conservative. The enclosure and collimated cases, in which the surface is a net absorber, are underpredicted, and the blade case is almost insensitive. Against Θ_G the deviations vanish at $\Theta_G = 0$ and decrease with h_g (panel b). The linearization of Equation (11) is exact for S2-L and agrees within about 25% for the other gas and enclosure cases (panel c) and fails for S3-L at large ε_{gray}, where the error exceeds a half. For collimated sources the error is governed by Φ, the normal absorptance for the source spectrum over ε_h (panel d); it turns non-conservative for Φ above about 1.2 at low ε_{gray}.

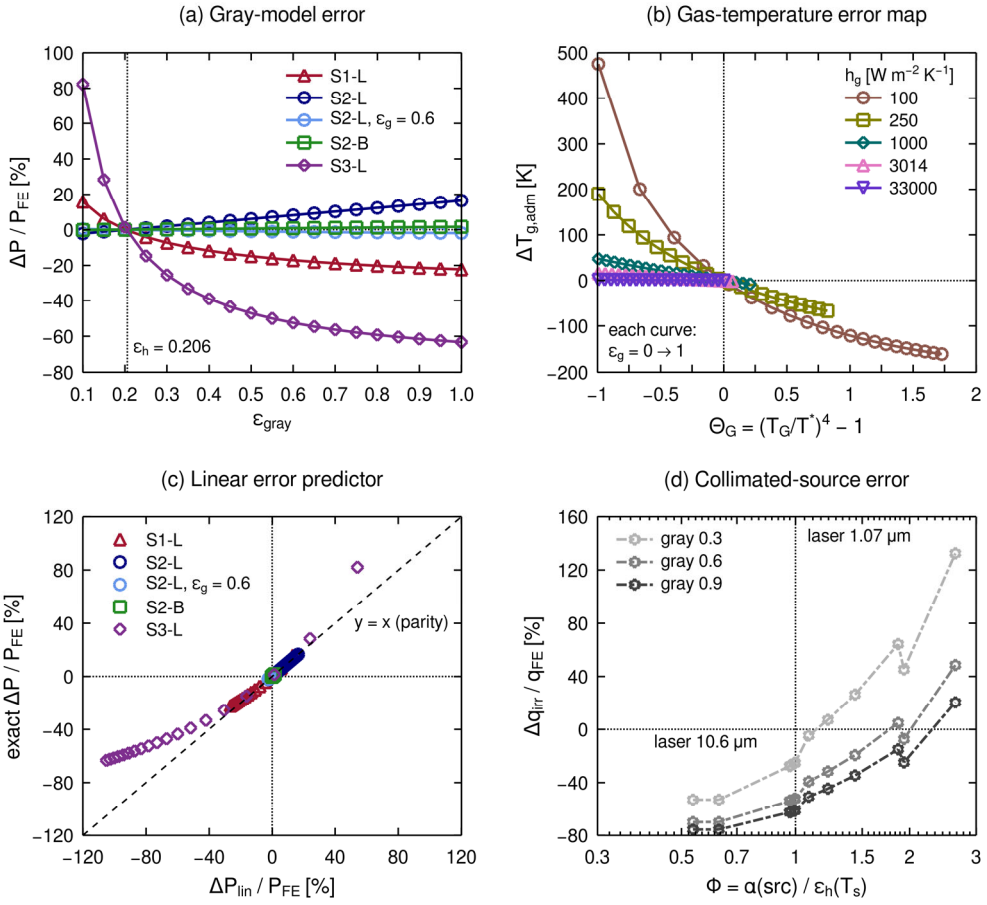

Figure 6. Gray-body error $\Delta P = P_{gray} - P_{FE}$ ($\gamma_{bc} = 3018$ cm^{-1}, $T_w = 300$ K); positive values are non-conservative. (**a**) $\Delta P/P_{FE}$ versus ε_{gray} for S1-L, S2-L, S2-L with $\varepsilon_g = 0.6$, S2-B and S3-L; vertical dotted line: ε_h. (**b**) $\Delta T_{g,adm}$ [K] for $\varepsilon_{gray} = 0.9$ (S2, BC-L) versus Θ_G for five h_g, with $\varepsilon_g = 0$–1 along each curve. (**c**) Exact versus linear estimate of Equation (11) for $\varepsilon_{gray} = 0.1$–1; dashed: parity. (**d**) $\Delta q_{irr}/q_{FE}$ for blackbody and laser sources (S3-L) versus Φ, for $\varepsilon_{gray} = 0.3$, 0.6 and 0.9. Dotted lines in (**b**–**d**): zero error, $\Theta_G = 0$ and $\Phi = 1$; the dash-dotted lines in (**d**) connect the computed points.

Two spectral effects cause the gray approximation to fail. The first is the structure of the emissivity. The Drude metal emits more at short wavelengths, the interference maxima occupy a few discrete bands, and the oxide phonon features lie in the long-wavelength tail. ε_h is therefore a Planck-weighted average that depends on temperature (Figure 4d). A single value cannot describe both the emission at the cap and the absorption of radiation from a source at another temperature. The second effect is short-wavelength absorption by

the metal. Interband transitions enhance it and drive Φ away from unity for hot sources (Section 3.7). Equation (11) gives the magnitude of the resulting error. It grows with the difference between $\varepsilon_{\mathrm{gray}}$ and ε_{h} and decreases with h_{g}.

3.7. Spectral Mismatch for Broadband Sources

Under broadband irradiation, the incident power is absorbed with the source spectrum but rejected with the 1050 K spectrum. In Figure 7, the upper panels use hemispherical absorptances, which isolate the spectral effect; $\Phi_{\mathrm{h}} = \alpha_{\mathrm{h}}/\varepsilon_{\mathrm{h}}$ is the mismatch for diffuse irradiation. The lower panels show the physical S3 calculation, a collimated beam at normal incidence absorbed with the normal absorptance. The absorbed spectrum is a density per unit wavelength (panel a) and moves toward the visible as T_{src} rises. With a Drude metal Φ_{h} stays within 10% of unity (panel b), and the collimated admissible irradiance is nearly independent of the source, varying by about ±8% across the Wiedemann–Franz interval (panel c). Interband absorption breaks this balance: Φ_{h} grows with T_{src}, and the irradiance limit falls by about 30% for a 2000 K source and by more than half for a 5800 K spectrum. The overshoot in panel (d) is the steady surface temperature predicted spectrally, minus T*, under the irradiance that a gray description with $\alpha = \varepsilon = \varepsilon_{\mathrm{h}}$ would admit. It stays between −18 and +4 K with the Drude metal and reaches 165 K with interband terms. The two metal descriptions are scenarios, since high-temperature near-infrared data for NiCrAlY are lacking and ultraviolet oxide absorption is neglected.

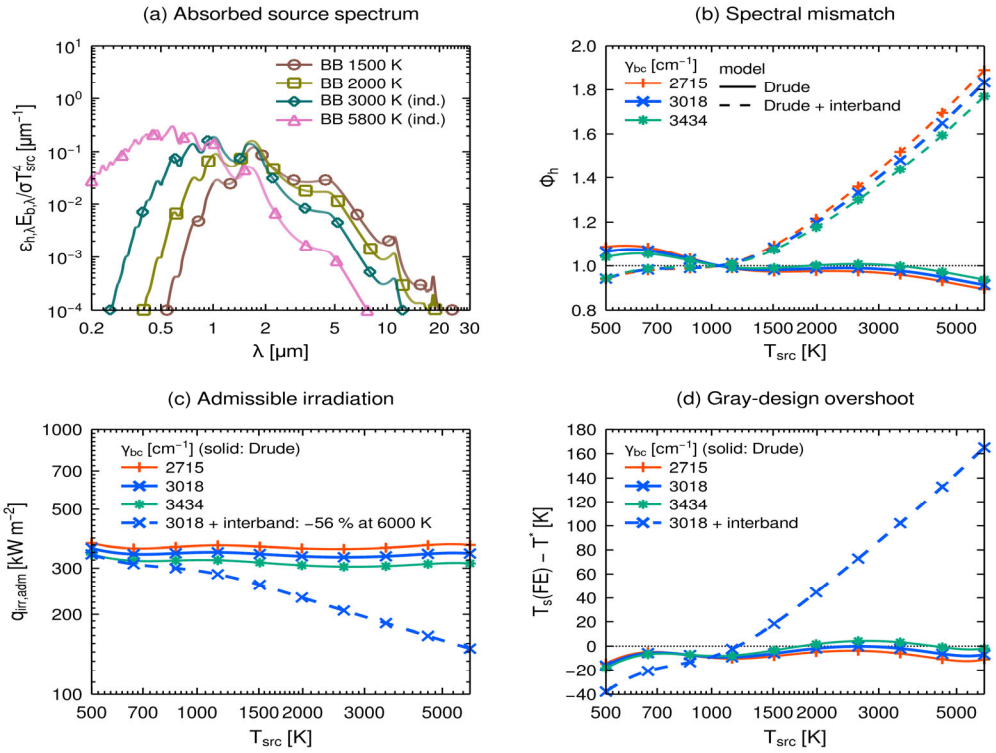

Figure 7. Spectral mismatch for broadband sources (optics at 1050 K; BC-L). (**a**) Absorbed spectrum $\varepsilon_{\mathrm{h},\lambda} E_{\mathrm{b},\lambda}/\sigma {T_{\mathrm{src}}}^4$ [$\mu\mathrm{m}^{-1}$] for blackbody sources at 1500–5800 K (hemispherical). (**b**) Φ_{h} versus T_{src} for three γ_{bc}, Drude (solid) and Drude + interband (dashed). (**c**) Admissible irradiance of a collimated beam at normal incidence (S3-L) versus T_{src}; dashed: with interband terms. (**d**) Overshoot T_{s}(FE) − T* under the gray-admitted irradiance (conditions of (**c**)). Dotted lines: $\Phi_{\mathrm{h}} = 1$ in (**b**) and T_{s}(FE) = T* in (**d**).

3.8. Transients and Radial Nonuniformity

After a step from $T_0 = 300$ K to P_{adm}, T_s of the one-dimensional reduced model first follows the semi-infinite $t^{1/2}$ law and then saturates on the scale τ_{th} (Figure 8a), from about 1.5 s for blade cooling to 19–33 s for the liner and collimated cases. In panel (b) the time t_{cross} at which the hottest point first reaches T^* falls by more than three orders of magnitude between a 1% and a three-hundred-fold overload x and moves from the lumped toward the semi-infinite limit. Panel (c) compares one-dimensional S2-L runs with optics updated continuously and frozen at 1050 K; they differ by less than 0.1 K. In the two-dimensional disk the rim, which exchanges heat by gray radiation, creates a radial nonuniformity (panel d). We measure it between the surface cells nearest to the axis (r_1) and to the edge (R); positive values mean a hotter center. It develops between R^2/α and a few τ_{th} and reaches 2–9 K at steady state, growing with the rim emissivity. This edge loss raises the two-dimensional gas-temperature limit (Section 3.9). All transients use variable-step BDF2, whose order and time-step error were verified separately (Section 2.6, Figure S2); the figure is not a convergence study.

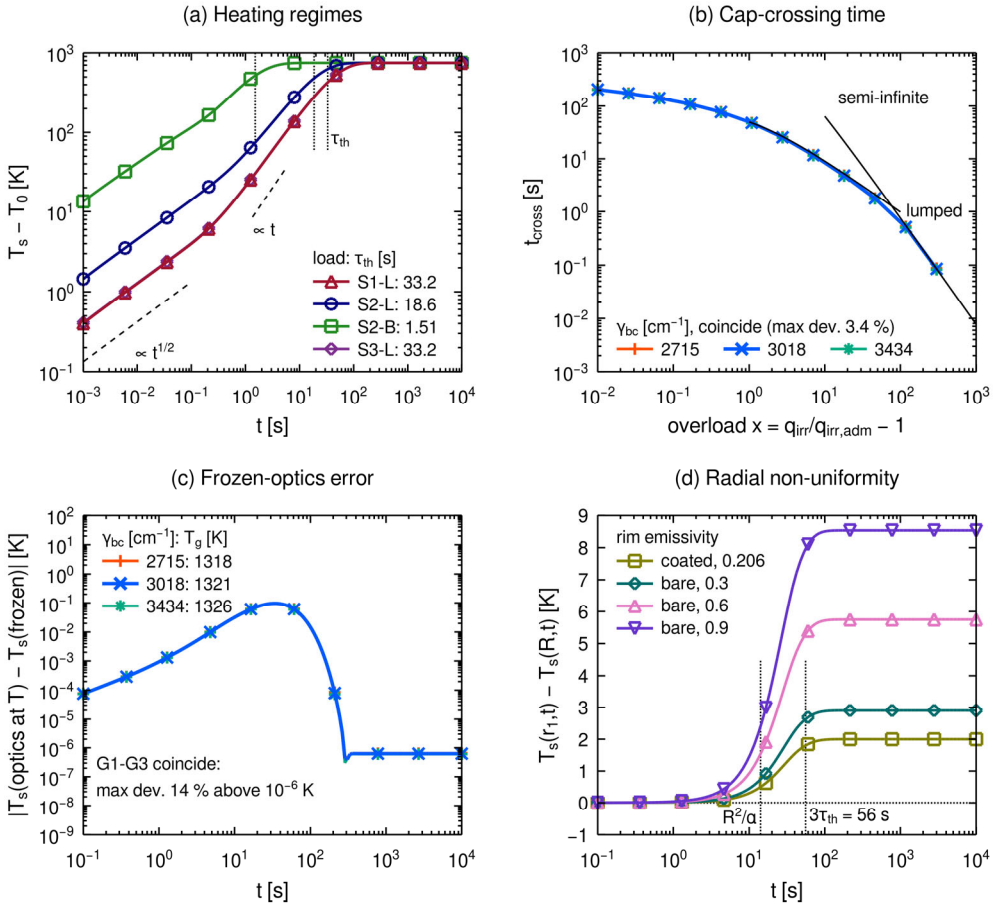

Figure 8. Transients after a step from $T_0 = 300$ K (variable-step BDF2). (**a**) $T_s - T_0$ of the one-dimensional reduced model after a step to P_{adm}; vertical lines: τ_{th}. (**b**) t_{cross} versus overload $x = q_{irr}/q_{irr,adm} - 1$ (S3-L, 2000 K blackbody) for three γ_{bc}, with lumped and semi-infinite limits. (**c**) $|T_s$(optics at T) − T_s(optics at 1050 K)| for one-dimensional S2-L. (**d**) $T_s(r_1, t) - T_s(R, t)$ of the two-dimensional disk (S2-L), r_1 and R being the innermost and outermost surface cell centers, for a coated rim and bare rims of emissivity 0.3, 0.6 and 0.9. In (**d**), horizontal dotted line: zero difference; vertical dotted lines: R^2/α and $3\tau_{th}$.

3.9. Robustness and Uncertainty of Admissible Thermal Loads

The load limits combine every element of the analysis, so their uncertainty has two components of different nature. Parametric uncertainty is described by the priors of Table S1. Structural uncertainty arises from modeling choices that have no probability distribution. Table 3 collects the limits for the two rim scenarios together with the Monte Carlo bands, and Table S2 lists the structural variants.

Table 3. Admissible loads per rim scenario and parametric bands ($\gamma_{bc} = 3018$ cm^{-1}).

Load	1D, Adiabatic Rim	2D, Gray Rim ($\varepsilon_{rim} = 0.6$)	2D/1D − 1	90% MC Band (1D)
S1-L: $T_{env,adm}$	1561 K	1664 K	+6.6%	1480–1647 K
S2-L: $T_{g,adm}$	1321 K	1398 K	+5.8%	1273–1366 K
S2-B: $T_{g,adm}$	1103.5 K	1106.1 K	+0.2%	1101.4–1105.1 K
S3-L: $q_{irr,adm}$	332 kW m^{-2}	431 kW m^{-2}	+29.8%	259–411 kW m^{-2}

MC band: 5–95% percentiles of 2000 samples with the Wiedemann–Franz prior for γ_{bc} (one-dimensional reduced model). S2-B is quoted with one more digit because its band is only a few kelvin wide. Structural variants are listed in Table S2 and are not included in the band.

For the enclosure and liner cases, the rim condition is the largest single source of difference between the reported values; for collimated irradiation, the graded interface has a comparable effect (Table S2). A gray rim acts as an additional heat sink. The limits then rise by about 6% for the enclosure and liner cases and by about 30% for collimated irradiation, but only by a fraction of a percent for the blade case, whose back face is cooled much more strongly. Neither rim treatment is a calibrated condition, so the two values span the scenarios considered, not the physically possible range.

Interface roughness and the choice of optical constants act mainly through the short-wavelength absorptance of the bond coat. For the convective cases, a 20 nm graded interface, nickel interband terms and the pure FPSQ wing each change P_{adm} by less than 1%, because convection dominates the top balance. The collimated load responds strongly: the graded interface lowers $q_{irr,adm}$ by 35%, the Névot–Croce factor [46] by 13% and interband absorption by 30%. The roughness amplitude is hypothetical and the two roughness models describe different structures [46,47], so these values measure the sensitivity to the assumption and do not define a bound.

The parametric bands are narrow for the convective cases and wide for the collimated one (Table 3). For the liner cases the variance is dominated by the back-face emissivity, which controls the heat rejected at the cooled face and hence q_b in Equation (10); the bond-coat damping matters only with the wide prior (Figure S3). At a base sample of 128 the Sobol indices identify the dominant factor but do not rank the minor ones. A 1% probability of exceeding the cap requires a back-off of a few percent for the convective and enclosure cases and of about a quarter for collimated irradiation. All these statements are conditional on the assumed intervals.

Several effects are negligible on the scale of these uncertainties: the anisotropy of Al_2O_3, its optical extrapolation above 928 K, the non-equilibrium emission bound Ξ, and the coating conductivities and boundary resistances (Table S2). The conclusions for the convective and enclosure cases therefore hold across all scenarios examined. The admissible collimated irradiance, in contrast, is known only to within a factor of about two, from roughly 0.2 to 0.43 MW m^{-2} for the variants considered.

4. Discussion

The results raise three questions that go beyond the individual figures: why a sub-micrometer stack controls the load capacity of a millimeter-thick component, what in this analysis is new, and how far its conclusions can be trusted.

4.1. Physical Interpretation

The stack decouples the two heat-transfer channels. Its conductive resistance is negligible against the substrate: the temperature drop across it stays below 0.05 K at all limit states, and the substrate fixes the conductive path. The radiative boundary condition, by contrast, is set entirely by the stack. The oxides are nearly transparent where most of the Planck power lies at the cap. The emission originates in the skin of the lossy bond coat, whose absorption is enhanced at the interference maxima created by the dielectric spacers. The oxides thus act as phase layers, not as emitters, and their thicknesses tune the position of the first order relative to the Planck peak. This mechanism differs from the insulation of a conventional top coat, which relies on low conductivity over hundreds of micrometers.

The same separation explains the small difference between the reduced and resolved coating descriptions (Figure S2). In the resolved case the net radiative exchange takes place in the metal skin below the transparent oxides. These layers therefore carry the conducted flux minus the net absorbed radiation, whereas the reduced model routes the whole flux through the lumped resistance. The resulting shift in T_s is the product of this absorbed flux and the oxide resistance; it is of order 10 mK and has the sign of the net exchange.

The direction in which the optics shifts P_{adm} depends on the role of radiation in the top balance. When the surface is a net emitter, as for a liner exposed to a transparent gas, a higher emissivity removes heat and raises the limit. When it is a net absorber, as in an enclosure or under collimated irradiation, a higher absorptance adds heat and lowers it. The gray-body error inherits this structure, and Θ_G identifies the regime from the irradiation temperature alone.

For design, the results suggest a short sequence. First, the case is classified by its irradiation temperature: if T_G lies below the cap, as for a liner exposed to an optically thin gas, any gray emissivity chosen larger than the spectral value is non-conservative, and the spectral value should be computed for the actual stack. Second, for enclosures and broadband sources, where the surface is a net absorber, the gray approximation errs on the safe side, provided the source spectrum does not overlap strong absorption in the metal; for short-wavelength sources this proviso has to be checked against interband data. Third, the margin to the cap is set from the parametric bands of Table 3 and, separately, from the structural variants, because the two do not combine into one probability. For the present stack this sequence leads to a back-off of a few percent for convective and enclosure heating and of about a quarter or more for collimated irradiation.

4.2. Originality and Scientific Contribution

The individual methods are established: Parratt and transfer-matrix optics, the indirect Kirchhoff formulation of thermal emission, finite-volume conduction with enthalpy and Kapitza resistances, and variance-based sensitivity analysis. Their application to another system is not claimed as methodological novelty. The contribution lies in their combination into a single chain, from temperature-dependent dielectric functions to load limits under a surface cap. The limit is obtained directly from the Kirchhoff transform of the substrate and verified against time-marched solutions. The linearized gray-error relation of Equation (11) is elementary, but it makes the sign of the error explicit through Θ_G.

The chain itself is not specific to the present materials. With other dielectric functions, conductivities and boundary conditions, it applies to further sub-micrometer oxide stacks

on metals, such as a thermally grown scale alone or a diffusion barrier, provided the films remain planar and optically coherent and the substrate opaque.

The physical results are specific to the nanometric stack. Its conductive and optical roles separate. The bond coat is the emitter and the oxides are phase layers. The gray-body error depends on the radiative regime under the cap. Convective and enclosure cases are insensitive to the open modeling choices, whereas collimated irradiation is not. Reporting the limits per rim scenario, with parametric and structural uncertainty kept apart, is intended to make these conclusions checkable.

4.3. Comparison with Theoretical Literature

Most radiative analyses of thermal barrier coatings treat thick, semitransparent zirconia layers, in which internal radiation transports heat through a top coat that also provides the conductive resistance [4]. The present stack lies in the opposite limit: it is optically thin, coherent and conductively negligible, so the relevant physics is interference above a metal rather than volumetric radiative transfer. The finding that the optical constants of the coating material control the radiative exchange is consistent with the emphasis placed on absorption in radiation-barrier materials [5], although the HEO-Z optics used here are a surrogate.

The two regimes also differ in how radiation reaches the metal. In a thick, semitransparent top coat, radiation transmitted to the bond coat can raise the metal temperature above the value set by conduction alone [4]. In the present stack this path is closed: the bond coat is opaque across the Planck band, and the net radiative flux reaching the substrate is a few 10^{-4} of the conducted flux at all limit states (Figure 3a).

The equivalence between direct and indirect emission calculations reported for layered media with nonuniform temperature [15] is reproduced numerically by the present implementation. The *p*-polarized feature near the alumina epsilon-near-zero frequency is consistent with the classical description of the Berreman mode of thin polar films [45]. The thermal boundary resistances assumed here lie within the ranges reported for metal–metal and metal–dielectric interfaces [10,11] (for the oxide–oxide interface R_1 this is an assumption), and their effect on the limits is negligible because the substrate dominates the conductive path. The low conductivity that motivates high-entropy zirconates [6] matters for thick coatings but has no effect at a film thickness of 200 nm. No theoretical study of the same stack and boundary conditions was found that would allow a direct quantitative comparison, so the numerical credibility rests on the benchmarks of Section 2.6.

4.4. Sensitivity and Uncertainty

The sensitivity analysis distinguishes inputs that matter from inputs that are uncertain. The back-face emissivity dominates the parametric variance of the liner loads because it controls the heat rejected at the cooled face, whereas the coating properties hardly matter despite their large intervals. The bond-coat damping becomes relevant only with the wide prior, which also covers a Lorenz number different from L_0; the Wiedemann–Franz prior is thus conditional on the free-electron value. The Sobol indices are estimated with sizable sampling error, and the bootstrap intervals are approximate, so only the identification of the dominant factor is supported.

The same ranking indicates which measurements would narrow the bands most efficiently. For the liner cases, the emissivity of the cooled back face at the operating temperature is the decisive input, whereas the coating optics enter only weakly. For collimated irradiation, the decisive quantity is the near-infrared absorptance of the bond coat at the cap, which governs the structural spread through roughness and interband absorption.

The structural uncertainty is larger than the parametric one under collimated irradiation. For the enclosure and liner cases, the rim scenario alone shifts the limits by about 6%, slightly beyond the 90% parametric bands, whereas the other structural variants stay within about 2%. Rim condition, roughness and interband absorption are not probabilistic and are not combined into a single band, because no information is available to weight them. Their spread should be read as the sensitivity of the prediction to these choices, not as a confidence interval. Extrapolations of the Al_2O_3 optics beyond 928 K and of the material tables beyond their validity range are likewise sources of uncertainty rather than established properties, although their quantified effect on the results is small.

These conditions also restrict the practical use of the predicted loads. The back-face emissivity, the rim condition, the interface roughness and the interband absorption of the bond coat are not calibrated properties of a component. They enter as intervals or as scenarios, without an assumed probability distribution [48]. The emissivity of nickel-based alloys changes during oxidation [49,50], and oxidation and roughness both raise the emissivity of metal surfaces [51]. For convection and enclosure irradiation, the limits can serve as estimates with a small margin, within these assumptions. For collimated irradiation, the limit gives only the order of magnitude and the direction of the effects. A design value would require the measured back-face emissivity, the roughness of the deposited interfaces and the near-infrared absorptance of the bond coat at the operating temperature.

4.5. Model Limitations

The main limitations follow from the inputs. The HEO-Z optics are a single-oscillator surrogate of cubic zirconia, and the plasma frequency of pure nickel is applied to both alloys. Bulk optical and thermal properties are applied to films of 200–500 nm, in which grain-boundary and surface scattering could raise the electronic damping. The Al_2O_3 optics are extrapolated above 928 K, with a small quantified effect, and the interband description uses room-temperature nickel parameters.

The geometric and boundary-condition idealizations are equally important. The interfaces are planar and coherent, and roughness enters only through two variants. The gas is gray and optically thin, the rim condition is a scenario, and the interior radiation of the blade back face is an assumption. The two-dimensional solution and its three-dimensional reconstruction are restricted to axisymmetric heating, and each sublayer is assumed to be in local thermodynamic equilibrium. Within these limits the analysis predicts trends and orders of magnitude. Quantitative use for a specific component would require the optical constants and interface structure of the actual coating.

The optical inputs do not affect the results equally. Where most of the power is emitted, the HEO-Z film acts mainly through its refractive index, which ε_∞ ties to measured data for yttria-stabilized zirconia [27]. Its phonon band lies in the long-wavelength tail. The surrogate omits absorption by the rare-earth dopants, which is measured in rare-earth-doped zirconates [52], and by defects; this absorption would act mainly under collimated irradiation. For the liner cases, the coating optics enter only weakly (Section 4.4). Film constants can also differ from bulk values; for Al_2O_3 films they depend on the deposition conditions [53]. Four results are robust: the separation of the conductive and radiative roles of the stack, the opacity of the bond coat, the sign rule of the gray-body error (Equation (11)) and the different sensitivity of the convective and collimated cases. The value of ε_h, the positions of the interference orders and the collimated limits depend on the model and are estimates for the stated inputs.

Real coatings differ in two further respects. Practical bond coats are much thicker than the present film. Since the reflectance saturates once the bond coat is opaque (Figure 3b), it remains the emitter, but its roughness and oxidation state become controlling inputs. The

predictions can be tested by measuring the spectral directional emissivity of coated coupons at the cap temperature, as done for nickel [54], and the infrared optical constants of the deposited films.

A further limitation concerns time. The coating is treated as chemically and structurally frozen, whereas in service the alumina scale thickens, the bond coat loses aluminum and the oxides sinter. Each of these processes shifts the interference order and the absorption of the metal skin; the thickness map of Figure S1d indicates the direction of the change but not its rate, which would require a growth law for the thermally grown oxide.

5. Conclusions

We examined how a 0.9 μm HEO-Z/Al_2O_3/NiCrAlY stack affects the admissible thermal loads of a Nimonic 80A disk under a 1050 K surface cap. The approach links temperature-dependent dielectric functions, coherent layer-resolved emission and finite-volume conduction. The central physical result is that the stack controls the surface radiation while leaving conduction unchanged. Its emissivity enhancement arises from interference above an opaque, lossy bond coat, which is the actual emitter, and its variation with T is set by the Planck weighting rather than by the material response. The novelty lies in carrying the coherent emission of the stack through the surface energy balance to the admissible load, which separates the conductive and radiative roles of a sub-micrometer coating and fixes the sign of the gray-body error from the radiative regime at the cap. These conclusions are theoretical and refer to the disk, stack, boundary conditions and surface cap defined in Section 2.1.

The analysis also shows when gray-body design rules fail. Under a surface cap, the sign of this error is fixed by whether the irradiation temperature lies below or above it. A gray emissivity larger than the spectral value is therefore non-conservative for convective heating by an optically thin gas, where the surface is a net emitter. It is conservative for enclosures and broadband irradiation, unless the source spectrum favors absorption by the metal.

The supplementary analyses support these findings from three sides. The thickness map shows that the baseline stack is not an emissivity optimum: without the alumina layer ε_h would rise from 0.21 to about 0.26, yet the gas-temperature limit of S2-L would gain less than 15 K, and the alumina scale required by the system would be lost. The conduction solver reproduces the analytical benchmarks to round-off, with second-order convergence in space and time, and the resolved and reduced coating descriptions differ by at most about 11 mK at steady state, so the numerical errors are far below the differences between the cases. The Monte Carlo analysis translates the sampled priors into back-offs of 6.3% (S1-L), 4.2% (S2-L), 0.2% (S2-B) and 26.9% (S3-L) for a 1% probability of exceeding the cap, with the back-face emissivity as the dominant parametric factor for the liner.

The conclusions for convective and enclosure heating hold across the rim, roughness and optical variants examined. Those for collimated irradiation depend on assumptions that remain open: the rim condition, the interface roughness and the interband absorption of the bond coat. The study thus provides a verified chain from optical constants to admissible loads. It also identifies the inputs whose improvement would most reduce the uncertainty: the infrared optical constants of multi-rare-earth-doped zirconia, a roughness description tied to a deposition route, and a temperature-dependent interband description of the bond coat. With these inputs, the same chain could set the surface-temperature margin of a coated component directly from its measured optical constants, instead of from an assumed gray emissivity.

Supplementary Materials: The following supporting information can be downloaded at: https://www.mdpi.com/article/10.3390/nano16231561/s1, Figure S1: Supplementary optical results and temperature field; Figure S2: Verification of the conduction solver; Figure S3: Uncertainty analysis (one-dimensional reduced model); Table S1: Uniform priors of the 15 Monte Carlo factors; Table S2: Structural variants and their effect on the admissible loads.

Author Contributions: Conceptualization, M.D. and L.B.; methodology, M.D. and L.B.; software, L.B.; validation, M.D.; formal analysis, M.D. and L.B.; investigation, M.D. and L.B.; data curation, M.D.; visualization, L.B.; writing—original draft preparation, M.D. and L.B.; writing—review and editing, M.D. and L.B.; supervision, M.D.; project administration, M.D. All authors have read and agreed to the published version of the manuscript.

Funding: This work was carried out through the Core Program within the National Research Development and Innovation Plan 2022–2027, carried out with the support of the Romanian Ministry of Research, Innovation and Digitalization (MCID), Contract No.: 5N/2023, Project Number: PN 23250101 part of Core Program acronym ENERCLEAN.

Data Availability Statement: The numerical data supporting the findings of this study are available from the corresponding author upon reasonable request. The simulation code is not publicly available.

Conflicts of Interest: The authors declare no conflicts of interest.

Abbreviations

The following abbreviations are used in this manuscript:

BC-L, BC-B	Liner and blade back-face cooling conditions
BDF2	Second-order backward differentiation formula
BE, CN	Backward (implicit) Euler and Crank–Nicolson time stepping
DC	Direct current
FE	Fluctuational electrodynamics (nongray model)
FPSQ	Four-parameter semi-quantum (dielectric model)
HEO-Z	Lanthanum-, samarium-, gadolinium-, neodymium- and ytterbium-doped zirconia
IB	Interband (absorption)
IR	Infrared
LO, TO	Longitudinal and transverse optical (phonon modes)
MC	Monte Carlo
S1, S2, S3	Load cases: enclosure, gas convection, collimated irradiation
TGO	Thermally grown oxide
WF	Wiedemann–Franz
YSZ	Yttria-stabilized zirconia

References

1. Padture, N.P.; Gell, M.; Jordan, E.H. Thermal barrier coatings for gas-turbine engine applications. *Science* **2002**, *296*, 280. [CrossRef] [PubMed]
2. Clarke, D.R.; Oechsner, M.; Padture, N.P. Thermal-barrier coatings for more efficient gas-turbine engines. *MRS Bull.* **2012**, *37*, 891. [CrossRef]
3. Vaßen, R.; Bakan, E.; Mack, D.E.; Guillon, O. A perspective on thermally sprayed thermal barrier coatings: Current status and trends. *J. Therm. Spray Technol.* **2022**, *31*, 685–698. [CrossRef]
4. Siegel, R. Internal radiation effects in zirconia thermal barrier coatings. *J. Thermophys. Heat Transf.* **1996**, *10*, 707. [CrossRef] [PubMed]
5. Koutsakis, G.; Clarke, D.R. Optical absorption effects in thermal radiation barrier coating materials. *Surf. Coat. Technol.* **2024**, *487*, 130974. [CrossRef]
6. Liu, D.; Shi, B.; Geng, L.; Wang, Y.; Xu, B.; Chen, Y. High-entropy rare-earth zirconate ceramics with low thermal conductivity for advanced thermal-barrier coatings. *J. Adv. Ceram.* **2022**, *11*, 961. [CrossRef]
7. Vakilifard, H.; Shahbazi, H.; Liberati, A.C.; Nair Saraswathy, R.B.; Lima, R.S.; Pugh, M.D.; Moreau, C. High entropy oxides as promising materials for thermal barrier topcoats: A review. *J. Therm. Spray Technol.* **2024**, *33*, 447–470. [CrossRef]
8. Swartz, E.T.; Pohl, R.O. Thermal boundary resistance. *Rev. Mod. Phys.* **1989**, *61*, 605. [CrossRef]

9. Cahill, D.G.; Braun, P.V.; Chen, G.; Clarke, D.R.; Fan, S.; Goodson, K.E.; Keblinski, P.; King, W.P.; Mahan, G.D.; Majumdar, A.; et al. Nanoscale thermal transport. II. 2003–2012. *Appl. Phys. Rev.* **2014**, *1*, 011305. [CrossRef]
10. Gundrum, B.C.; Cahill, D.G.; Averback, R.S. Thermal conductance of metal-metal interfaces. *Phys. Rev. B* **2005**, *72*, 245426. [CrossRef]
11. Blank, M.; Weber, L. Towards a coherent database of thermal boundary conductance at metal/dielectric interfaces. *J. Appl. Phys.* **2019**, *125*, 095302. [CrossRef]
12. Born, M.; Wolf, E. *Principles of Optics*, 7th ed.; Cambridge University Press: Cambridge, UK, 1999. [CrossRef]
13. Polder, D.; Van Hove, M. Theory of radiative heat transfer between closely spaced bodies. *Phys. Rev. B* **1971**, *4*, 3303. [CrossRef]
14. Greffet, J.-J.; Nieto-Vesperinas, M. Field theory for generalized bidirectional reflectivity: Derivation of Helmholtz's reciprocity principle and Kirchhoff's law. *J. Opt. Soc. Am. A* **1998**, *15*, 2735. [CrossRef]
15. Wang, L.P.; Basu, S.; Zhang, Z.M. Direct and indirect methods for calculating thermal emission from layered structures with nonuniform temperatures. *J. Heat Transf.* **2011**, *133*, 072701. [CrossRef]
16. Parratt, L.G. Surface studies of solids by total reflection of X-rays. *Phys. Rev.* **1954**, *95*, 359. [CrossRef]
17. Katsidis, C.C.; Siapkas, D.I. General transfer-matrix method for optical multilayer systems with coherent, partially coherent, and incoherent interference. *Appl. Opt.* **2002**, *41*, 3978. [CrossRef] [PubMed]
18. Byrnes, S.J. Multilayer optical calculations. *arXiv* **2016**, arXiv:1603.02720. [CrossRef]
19. Manara, J.; Arduini-Schuster, M.; Rätzer-Scheibe, H.-J.; Schulz, U. Infrared-optical properties and heat transfer coefficients of semitransparent thermal barrier coatings. *Surf. Coat. Technol.* **2009**, *203*, 1059–1068. [CrossRef]
20. Eldridge, J.I.; Spuckler, C.M. Determination of scattering and absorption coefficients for plasma-sprayed yttria-stabilized zirconia thermal barrier coatings. *J. Am. Ceram. Soc.* **2008**, *91*, 1603–1611. [CrossRef]
21. Baranov, D.G.; Xiao, Y.; Nechepurenko, I.A.; Krasnok, A.; Alù, A.; Kats, M.A. Nanophotonic engineering of far-field thermal emitters. *Nat. Mater.* **2019**, *18*, 920–930. [CrossRef] [PubMed]
22. Gervais, F.; Piriou, B. Anharmonicity in several-polar-mode crystals: Adjusting phonon self-energy of LO and TO modes in Al_2O_3 and TiO_2 to fit infrared reflectivity. *J. Phys. C Solid State Phys.* **1974**, *7*, 2374. [CrossRef]
23. Zeidler, S.; Posch, T.; Mutschke, H. Optical constants of refractory oxides at high temperatures. *Astron. Astrophys.* **2013**, *553*, A81. [CrossRef]
24. Lucarini, V.; Peiponen, K.-E.; Saarinen, J.J.; Vartiainen, E.M. *Kramers–Kronig Relations in Optical Materials Research*; Springer Series in Optical Sciences, Volume 110; Springer: Berlin/Heidelberg, Germany, 2005. [CrossRef]
25. Zhao, X.; Vanderbilt, D. Phonons and lattice dielectric properties of zirconia. *Phys. Rev. B* **2002**, *65*, 075105. [CrossRef]
26. Pecharromán, C.; Ocaña, M.; Serna, C.J. Optical constants of tetragonal and cubic zirconias in the infrared. *J. Appl. Phys.* **1996**, *80*, 3479. [CrossRef]
27. Wood, D.L.; Nassau, K. Refractive index of cubic zirconia stabilized with yttria. *Appl. Opt.* **1982**, *21*, 2978. [CrossRef] [PubMed]
28. Ordal, M.A.; Bell, R.J.; Alexander, R.W.; Long, L.L.; Querry, M.R. Optical properties of fourteen metals in the infrared and far infrared: Al, Co, Cu, Au, Fe, Pb, Mo, Ni, Pd, Pt, Ag, Ti, V, and W. *Appl. Opt.* **1985**, *24*, 4493. [CrossRef] [PubMed]
29. Raj, S.V. *Thermophysical Properties of Cold and Vacuum Plasma Sprayed Cu-Cr-X Alloys, NiAl and NiCrAlY Coatings, Part 1: Electrical and Thermal Conductivity, Thermal Diffusivity, and Total Hemispherical Emissivity*; NASA/TM-2017-219715; NASA Glenn Research Center: Cleveland, OH, USA, 2017. Available online: https://ntrs.nasa.gov/api/citations/20170011293/downloads/20170011293.pdf (accessed on 9 November 2026).
30. Special Metals Corporation. *NIMONIC Alloy 80A*; Publication No. SMC-099; Special Metals Corporation: Huntington, WV, USA, 2004. Available online: https://www.specialmetals.com/documents/technical-bulletins/nimonic-alloy-80A.pdf (accessed on 9 November 2026).
31. Rakić, A.D.; Djurišić, A.B.; Elazar, J.M.; Majewski, M.L. Optical properties of metallic films for vertical-cavity optoelectronic devices. *Appl. Opt.* **1998**, *37*, 5271. [CrossRef] [PubMed]
32. Munro, R.G. Evaluated material properties for a sintered α-alumina. *J. Am. Ceram. Soc.* **1997**, *80*, 1919–1928. [CrossRef]
33. Raj, S.V. *Thermophysical Properties of Cold and Vacuum Plasma Sprayed Cu-Cr-X Alloys, NiAl and NiCrAlY Coatings, Part 2: Specific Heat Capacity*; NASA/TM-2017-219716; NASA Glenn Research Center: Cleveland, OH, USA, 2017. Available online: https://ntrs.nasa.gov/api/citations/20170011294/downloads/20170011294.pdf (accessed on 9 November 2026).
34. Cappella, A.; Battaglia, J.-L.; Schick, V.; Kusiak, A.; Lamperti, A.; Wiemer, C.; Hay, B. High temperature thermal conductivity of amorphous Al_2O_3 thin films grown by low temperature ALD. *Adv. Eng. Mater.* **2013**, *15*, 1046. [CrossRef]
35. Modest, M.F. *Radiative Heat Transfer*, 3rd ed.; Academic Press: Oxford, UK, 2013.
36. Shamsundar, N.; Sparrow, E.M. Analysis of multidimensional conduction phase change via the enthalpy model. *J. Heat Transf.* **1975**, *97*, 333. [CrossRef]
37. Carslaw, H.S.; Jaeger, J.C. *Conduction of Heat in Solids*, 2nd ed.; Clarendon Press: Oxford, UK, 1959.
38. Patankar, S.V. *Numerical Heat Transfer and Fluid Flow*; Hemisphere: New York, NY, USA, 1980.
39. LeVeque, R.J. *Finite Difference Methods for Ordinary and Partial Differential Equations*; SIAM: Philadelphia, PA, USA, 2007. [CrossRef]

40. Tiesinga, E.; Mohr, P.J.; Newell, D.B.; Taylor, B.N. CODATA recommended values of the fundamental physical constants: 2018. *Rev. Mod. Phys.* **2021**, *93*, 025010. [CrossRef] [PubMed]
41. Saltelli, A.; Annoni, P.; Azzini, I.; Campolongo, F.; Ratto, M.; Tarantola, S. Variance based sensitivity analysis of model output. Design and estimator for the total sensitivity index. *Comput. Phys. Commun.* **2010**, *181*, 259. [CrossRef]
42. Jansen, M.J.W. Analysis of variance designs for model output. *Comput. Phys. Commun.* **1999**, *117*, 35. [CrossRef]
43. Puy, A.; Becker, W.; Lo Piano, S.; Saltelli, A. A comprehensive comparison of total-order estimators for global sensitivity analysis. *Int. J. Uncertain. Quantif.* **2022**, *12*, 1–18. [CrossRef]
44. Kats, M.A.; Blanchard, R.; Genevet, P.; Capasso, F. Nanometre optical coatings based on strong interference effects in highly absorbing media. *Nat. Mater.* **2013**, *12*, 20–24. [CrossRef] [PubMed]
45. Berreman, D.W. Infrared absorption at longitudinal optic frequency in cubic crystal films. *Phys. Rev.* **1963**, *130*, 2193. [CrossRef]
46. Névot, L.; Croce, P. Caractérisation des surfaces par réflexion rasante de rayons X. Application à l'étude du polissage de quelques verres silicates. *Rev. Phys. Appl.* **1980**, *15*, 761. [CrossRef]
47. Bruggeman, D.A.G. Berechnung verschiedener physikalischer Konstanten von heterogenen Substanzen. I. Dielektrizitätskonstanten und Leitfähigkeiten der Mischkörper aus isotropen Substanzen. *Ann. Phys.* **1935**, *416*, 636. [CrossRef]
48. Roy, C.J.; Oberkampf, W.L. A comprehensive framework for verification, validation, and uncertainty quantification in scientific computing. *Comput. Methods Appl. Mech. Eng.* **2011**, *200*, 2131–2144. [CrossRef]
49. Kobayashi, M.; Ono, A.; Otsuki, M.; Sakate, H.; Sakuma, F. A database of normal spectral emissivities of metals at high temperatures. *Int. J. Thermophys.* **1999**, *20*, 299–308. [CrossRef]
50. Li, L.; Wang, F.; Gao, J.; Yu, K.; Wang, L.; Liu, Y. Accurately measuring the infrared spectral emissivity of Inconel 601, Inconel 625, and Inconel 718 alloys during the oxidation process. *Sensors* **2024**, *24*, 5906. [CrossRef] [PubMed]
51. Jo, H.; King, J.L.; Blomstrand, K.; Sridharan, K. Spectral emissivity of oxidized and roughened metal surfaces. *Int. J. Heat Mass Transf.* **2017**, *115*, 1065–1071. [CrossRef]
52. Champagne, V.K., III; Pisaturo, G.; Clarke, D.R. High temperature oxides for selective absorption of thermal radiation. *J. Eur. Ceram. Soc.* **2023**, *43*, 7656–7667. [CrossRef]
53. Kischkat, J.; Peters, S.; Gruska, B.; Semtsiv, M.; Chashnikova, M.; Klinkmüller, M.; Fedosenko, O.; Machulik, S.; Aleksandrova, A.; Monastyrskyi, G.; et al. Mid-infrared optical properties of thin films of aluminum oxide, titanium dioxide, silicon dioxide, aluminum nitride, and silicon nitride. *Appl. Opt.* **2012**, *51*, 6789–6798. [CrossRef] [PubMed]
54. Setién-Fernández, I.; Echániz, T.; González-Fernández, L.; Pérez-Sáez, R.B.; Tello, M.J. Spectral emissivity of copper and nickel in the mid-infrared range between 250 and 900 °C. *Int. J. Heat Mass Transf.* **2014**, *71*, 549–554. [CrossRef]

Disclaimer/Publisher's Note: The statements, opinions and data contained in all publications are solely those of the individual author(s) and contributor(s) and not of MDPI and/or the editor(s). MDPI and/or the editor(s) disclaim responsibility for any injury to people or property resulting from any ideas, methods, instructions or products referred to in the content.